Hindawi
Geofluids
Volume 2020, Article ID 4237163, 14 pages
https://doi.org/10.1155/2020/4237163

Research Article

Effect of Wetting-Drying Cycle on the Deformation and Seepage Behaviors of Rock Masses around a Tunnel

Qingzhen Guo,[1] Haijian Su,[1] Hongwen Jing,[1] and Wenxin Zhu[2]

[1]*State Key Laboratory for Geomechanics and Deep Underground Engineering, China University of Mining and Technology, Xuzhou, Jiangsu 221116, China*
[2]*School of Traffic and Civil Engineering, Shandong Jiaotong University, Jinan, Shandong 250357, China*

Correspondence should be addressed to Haijian Su; hjsu@cumt.edu.cn

Received 30 November 2019; Revised 12 May 2020; Accepted 15 May 2020; Published 26 May 2020

Academic Editor: Mohammad Sarmadivaleh

Water inrush caused by the wetting-drying cycle is a difficult problem in tunnel excavation. To investigate the effect of the wetting-drying cycle on the stability of the tunnel surrounding rock, physical experiments and numerical simulations regarding the process of tunnel excavation with different wetting-drying cycle numbers were performed in this study. The evolutions of stress, displacement, and pore water pressure were analyzed. With the increase in cycle number, the pore water pressure, vertical stress, and top-bottom approach of the tunnel surrounding rock increase gradually. And the increasing process could be divided into three stages: slightly increasing stage, slowly increasing stage, and sharply increasing stage, respectively. The failure process of the surrounding rock under the wetting-drying cycle gradually occurs from the roof to side wall, while the baseplate changes slightly. The simulation results showed that the maximum principal stress in the surrounding rock mass of the tunnel increases, while the minimum principal stress decreases. Furthermore, the displacement of the rock mass decreases gradually with the increasing distance from the tunnel surface. By comparing the simulation results with the experimental results, well consistency is shown. The results in this study can provide helpful references for the safe excavation and scientific design of a tunnel under the wetting-drying cycle.

1. Introduction

With the development of tunnel projects to mountainous terrain, the effect of the wetting-drying cycle on the surrounding rock mass has aroused the concern of many scholars. The water-rock interaction can affect the performance of a rock and then influence the stability of rock projects [1–4]. The wetting-drying cycle plays a significant role in many special types of engineering, such as the tunnel construction in the karst area, water level fluctuation in a reservoir or dam, and seasonal rainfall [5–7].

In order to solve these special engineering problems, many researchers performed many laboratory tests to study the effect of the wetting-drying cycle on the physical and mechanical properties of the rock mass, especially strength and deformation [8–11]. Summer and Loubser [12] studied the physical and mechanical properties of four groups of sandstone specimens with different water contents. The results clarified the weathering mechanism and control factors of sandstone under different wetting-drying moisture amplitudes. Coombers and Naylor [13] investigated the weathering mechanism of limestone, granite, concrete, and other materials with different wetting-drying cycle numbers through the scanning electron microscope (SEM). Jeng et al. [14] carried out the research on the mechanism of wetting deterioration of sandstone, such as strength and deformation. The results showed that the uniaxial compressive strength of sandstone decreases by 40%, and the elastic modulus decreases by 50% due to the wetting-drying cycle. Li et al. [15] investigated the influence of water content on the strength and deformation properties of metasandstone specimens through the triaxial compressive tests. They found that the influence of water on the deformability of tested rocks is reflected as a reduction of Young's modulus and increase of

Poisson's ratio, which indicates that the wet metasedimentary rocks will deform more than the dry ones under the same stress condition.

Besides, some model experiments and numerical simulations were conducted to study the overall stability of the tunnel surrounding rock under the effect of the wetting-drying cycle [16–18]. Yin et al. [19] revealed the mining-induced water-condition zone using theoretical studies and field measurements, and the generating condition of the hydraulic fractures was also obtained by the water pressure. Ma et al. [20] carried out a series of seepage-induced particle erosion experiments to study the effects of erosion seepage on the hydraulic properties of broken red sandstones. Experimental results showed that, as erosion seepage processes, porosity, and permeability of the specimen increase, the non-Darcy factor decreases. In addition, Ma et al. [21] also investigated the particle erosion effect on the water inrush mechanism of the karst collapse pillar (KCP) by using the $FLAC^{3D}$ numerical simulation. According to the simulation, the evolutions of shear stress field, seepage field, and plastic zone along were obtained, and some influencing factors of water inrush were analyzed. Yao et al. [22] proposed a fluid-solid coupling model for the karst collapse pillar based on the groundwater dynamics theory and seepage theory of porous media. Zhou et al. [23] carried out dynamic notched semicircular bending (NSCB) tests for dry and saturated sandstone specimens using a modified split Hopkinson pressure bar (SHPB) setup. Test results revealed that the dynamic fracture initiation, propagation toughness, and crack propagation velocity of the saturated specimen were apparently lower than those of the dry ones at the same loading rate. Bidgoli and Jing [24] evaluated the effect of water pressure on the strength and deformation parameters of the fractured rock mass through the discrete element method (DEM).

Most of the previous researches mainly focused on the slope stability and the evolution law of the fissures under the wetting-drying cycle. Few geomechanical model tests were carried out to study the instability failure behavior and water inrush of the tunnel surrounding rock under the effect of the wetting-drying cycle. In this study, the main mission is to investigate the stability problems of the surrounding rock under the wetting-drying cycle. Physical experiment model was set up based on the Liupanshan tunnel in Ningxia Province, China. The evolutions of pore water pressure, stress, and displacement under different cycle numbers were investigated according to the experimental results. In addition, relevant numerical simulations were also conducted to verify the model test results and compensate for the lack of test data. The principal stress distributions and deformation characteristics under the wetting-drying cycle are further revealed, providing a theoretical basis for the prevention and control of water inrush in underground engineering.

2. Physical Experiment

2.1. Engineering Geological Condition. The Liupanshan tunnel is located in the Qinglan expressway, the Ningxia Hui Autonomous Region. It is designed as a single-hole separated tunnel with a distance of 31-48 m between the left and right line. Through engineering calculation and analysis, the general inflow water through the tunnel is 17427.6 m^3/d, and the maximum inflow water is 37999.4 m^3/d. The surrounding rocks are mainly sandstone based on a field survey. Due to the geologic and engineering effects, the sandstone in the tunnel is not intact and contains various flaws, e.g., joint and crack. The surrounding rock permeates due to these joint and crack, resulting in the alternation action of wetting-drying. Large chunks of sandstone were collected at the tunnel site and brought back to the laboratory for experimental analysis. The XRD result (Figure 1(a)) shows that the main minerals in this tunnel are quartz, silica, dolomite, and calcite. From the XRF result (see Figure 1(b)), it is clear that the main compounds are SiO_2, CO_2, CaO, Al_2O_3, and MgO, accounting for 34.62%, 24.5%, 13.8%, 10.34%, and 7.88%, respectively. The prepared sandstone specimens, after a series of machining processes, were made for the conventional triaxial compressive test, with the diameter and height of 50 and 100 mm, respectively.

2.2. Similar Material and Similarity Ratio. In model experimental studies, the selection of materials and the ratio of similar material are very important. These factors not only determine whether the model can correctly reflect the characteristics of the prototype but also decide the degree of difficulty of model processing and smooth performance of test. Therefore, based on previous research results and full consideration of fluid-solid coupling characteristics, river sand and talcum powder were selected as aggregate materials, and paraffin and hydraulic oil were selected as cementing materials. The similar specimen was made using these materials in a rational ratio. The mix ratio of materials maintained the physical similarity as much as possible, such as density ρ, porosity Φ, uniaxial compressive strength σ_c, elastic modulus E_c, tensile strength σ_t, cohesion C, and internal friction φ_0.

The optimal material ratio was determined by a mixed-level orthogonal design test. According to the principle of the orthogonal test, the specimens with different proportions were designed and fabricated. After the specimens were prepared, the porosity and density were measured by a weighing method. More specifically, specimens of $\varphi 50 \times 100$ mm were used for uniaxial compressive tests to measure the uniaxial compressive strength σ_c and elastic modulus E_c, specimens of $\varphi 50 \times 25$ mm were used for Brazilian splitting tests to determine the tensile strength σ_t, and specimens of $\varphi 50 \times 50$ mm were used for shear tests to obtain cohesion C and internal friction φ_0. Based on extensive testing, a similar material composed of river sand, talcum powder, paraffin, and hydraulic oil at a mass ratio of 23.0 : 3.5 : 1.5 : 1.0 was used to simulate sandstone. The test method is based on the specification of "Engineering Rock Test Method Standard (GB/T 502666-2013)" [25]. According to the experimental data on rocks and similar materials, the physical and mechanical properties of sandstone and similar materials are listed in Table 1.

Some basic similarity requirements must be met in physical model tests, such as geometric, physical-mechanical properties, and boundary conditions. The ratio of the prototype parameters to model parameters is defined as the similarity ratio, which is usually a constant [26]. According

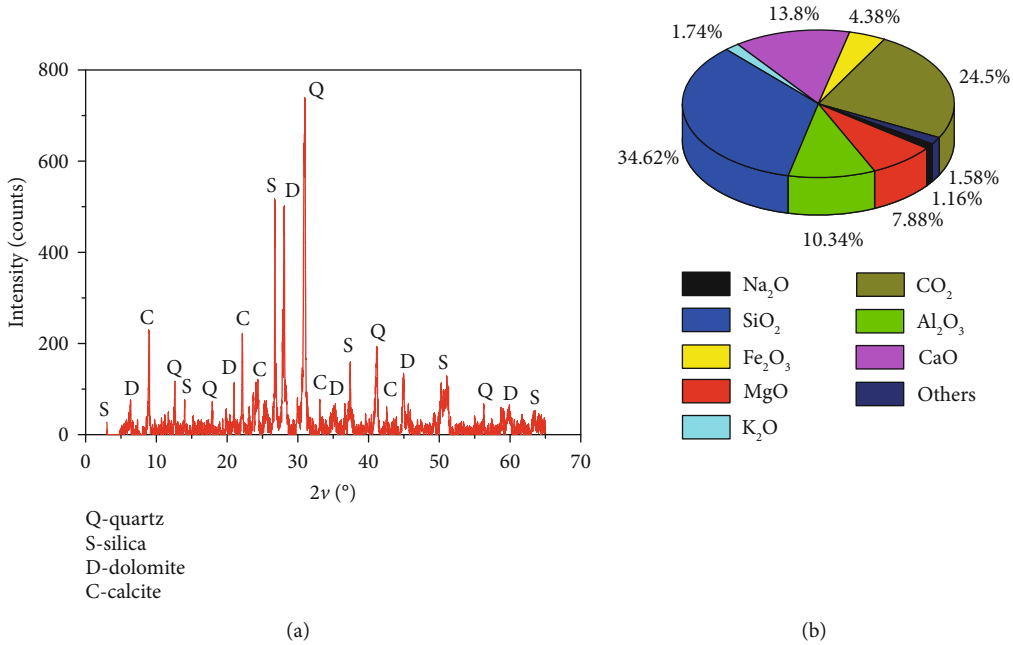

(a) (b)

Figure 1: Main components of the tested sandstone: (a) XRD and (b) XRF.

Table 1: Physical-mechanical properties of the prototype and similar material.

	ρ	Φ	σ_c	σ_t	E_c	C	φ_0
Sandstone	2.51 g/cm^3	8.27%	81.83 MPa	11.74 MPa	8.89 GPa	18.61 MPa	43.08°
Similar material	2.02 g/cm^3	8.73%	323.73 kPa	43.50 kPa	25.78 MPa	79.40 kPa	37.34°

to the engineering geological condition, the geometric similarity ratio and volume-weight similarity ratio in this model experiment are determined as 100 and 1.24, respectively [27–29].

2.3. Physical Experimental System. In order to explore the process and mechanism of water inrush in the karst area under the wetting-drying cycle, a set of visualization test systems for karst tunnel water inrush disaster was independently developed, as shown in Figure 2. The system mainly consists of a loading device, hydraulic loading system, and data acquisition system. The experimental framework is made of a seamless welded steel plate with a thickness of 12 mm, and the net size of the framework is 1000 × 1000 × 300 mm. The 5 cm apart bolt holes around the frame are reserved to connect the flange. And a transparent glass is equipped on the outside of flange to observe the deformation and failure process of the tunnel surrounding rock. In order to ensure the sealing performance between the glass plate and flange, a water-blocking rubber belt is embedded in the inner side of the bolt hole. In addition, the hydraulic loading system has the advantage of gas-liquid combination, which uses a group of nitrogen cylinder with servo control to provide pressure. Therefore, the water in the tank is driven to provide a stable water pressure for the water storage structure of the test system. According to the geometric relationship between the water storage structure and model tunnel, a section of a PVC pipe with an inner diameter of 50 mm is combined with a stripper rubber to simulate the water storage structure.

2.4. Model Test Condition and Production Procedure of Wetting-Drying Cycle. Figure 3 shows the simulated experimental condition of the tunnel surrounding rock under the effect of the wetting-drying cycle. The height and width of the tunnel are 72 mm and 110 mm, respectively. The bottom edge of the karst structure is 40 mm away from the tunnel vault. An osmotic pressure gauge, with the measuring range of 1 MPa, was arranged at 20 mm above the tunnel vault. The sensor of the osmotic gauge is cylindrical, with the diameter and length of 5 mm and 20 mm, respectively. The installing direction of the sensor is the same with that of water pressure loading. And the osmotic pressure gauge is connected to a computer via a fixed signal amplifier. Three pressure cells are distributed around the tunnel, as shown in Figure 3. These pressure cells, with the diameter and thickness of 17 and 8 mm, respectfully, have the maximum testing capacity of 1 MPa.

Figure 4 shows the production procedure of the physical model test, which can be divided into six steps, as follows:

Step 1: the components of a similar material were weighted separately in proportion before stirring. In order

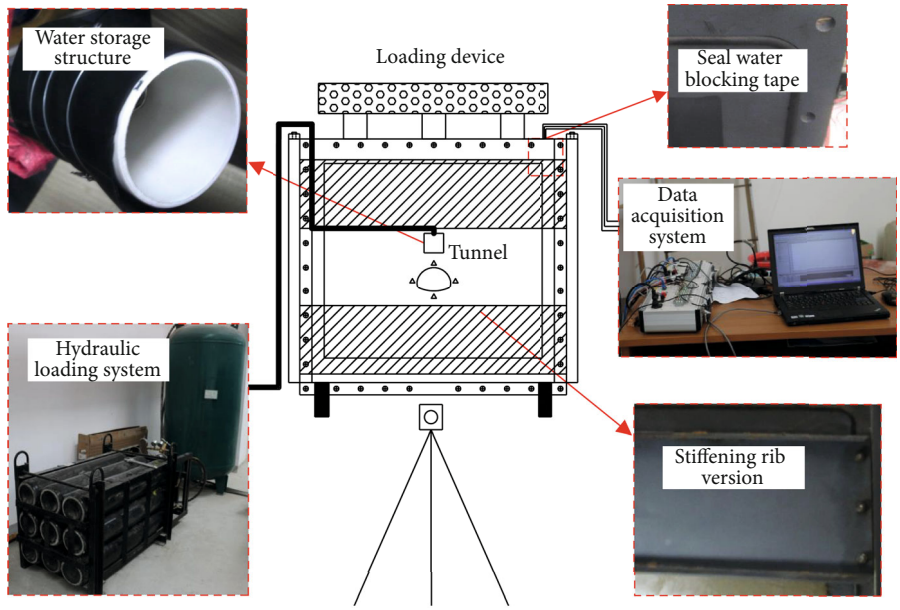

Figure 2: Experimental system of water inrush disasters for the karst tunnel.

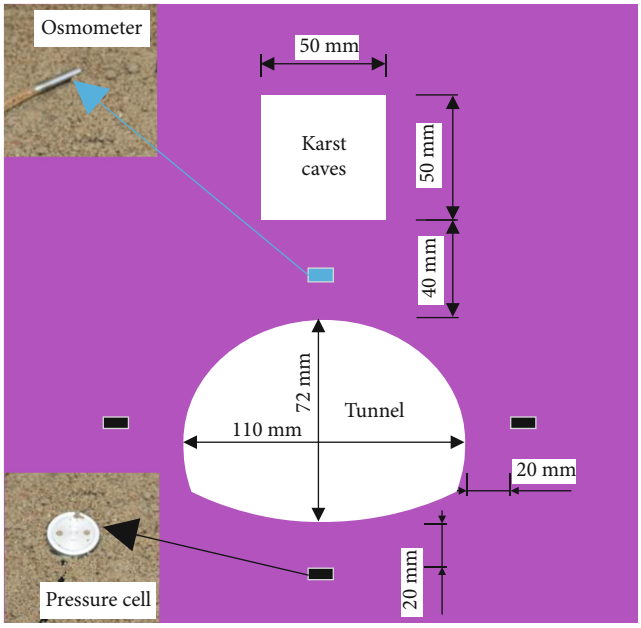

Figure 3: Model test condition.

to achieve uniform stirring, the talcum powder and river sand were firstly mixed evenly in the blender and the bottom of the blender was heated continuously meanwhile. Then, hydraulic oil and melted paraffin were added in the blender, which were stirred well with previous mixed materials

Step 2: in order to improve the accuracy of experimental data, the lubricating oil was brushed on the frame and loading plate to reduce the friction, as shown in Figure 4(a)

Step 3: the well-stirred similar materials were poured into a test bed in batches. The similar materials need to be vibrated and tamped one time every 10 cm thick to become tightly. What is more, water storage structure, pressure box, osmotic pressure gauge, and other sensors were buried, respectively, once similar materials were laid to the specified position, as shown in Figures 4(b)–4(d)

Step 4: after pouring similar materials, the model was kept for 48 hours to cool solidify. The loading device was installed on the upper part of the model with a specified in situ stress load applied

Step 5: tunnel excavation was carried out after 6 hours of constant in situ stress. Then, the displacement sensor was installed to measure the top-bottom approach of the tunnel. The displacement sensor is the series of KTR-G, with the stroke range and measurement accuracy of 25 and 0.01 mm, respectively. In order to reduce the error, the wetting-drying cycle was performed 6 hours after the installation of the displacement sensor, as shown in Figures 4(e) and 4(f). During this period, the connection and debugging of all the components, devices, and acquisition instruments were carried out

Step 6: the water pressure applied to the model was calculated through similarity calculation based on the field test data. As shown in Table 2, when the wetting-drying cycle number $N = 1$, the water pressure was increased from 0 to 0.03 MPa firstly; then, this pressure value was kept constant for 30 minutes before unloading. To reach the preset dry state, the model was kept for 120 minutes. In this process, the water in the storage structure will continue to flow out from the surrounding rock of the tunnel, which is actually a process of unloading water pressure. Therefore, the water pressure at the next cycle returns to zero, so as to simulate the wetting-drying cycle process of the tunnel surrounding rock. When $N = 2$, the water pressure was increased from 0 to 0.06 MPa, and the rest of process was

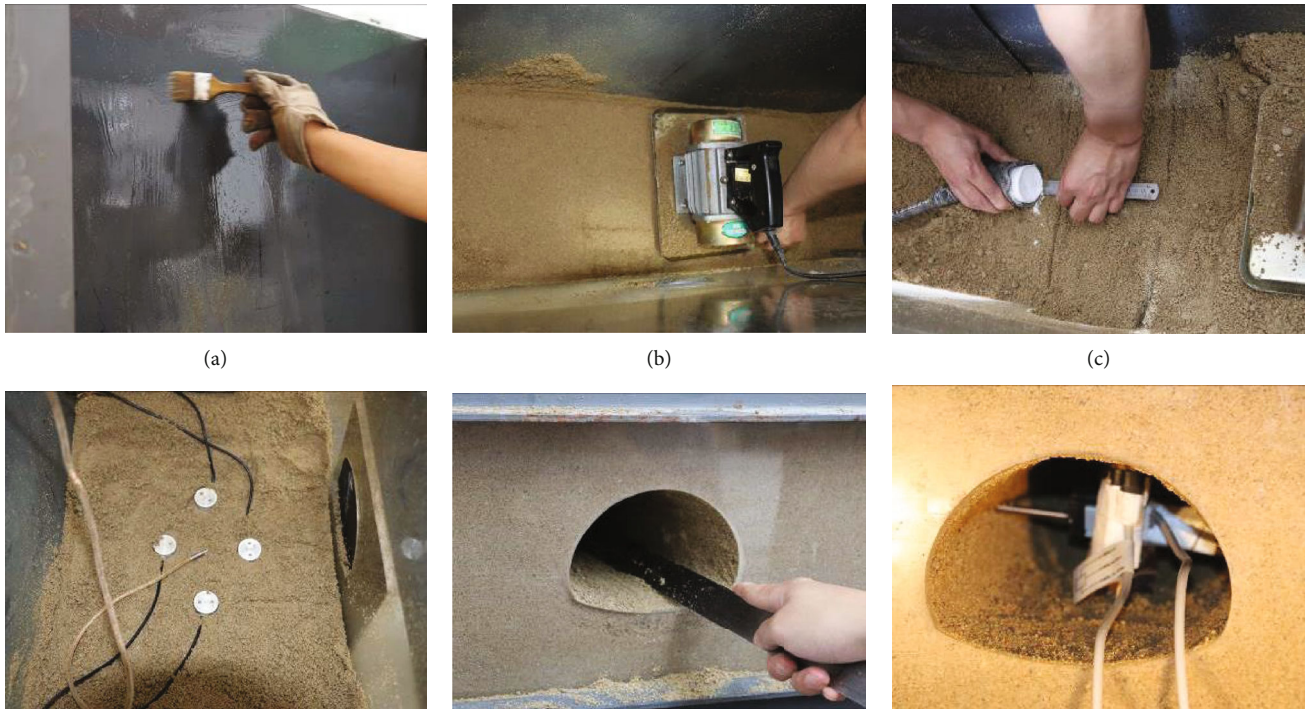

(a) (b) (c)

(d) (e) (f)

Figure 4: Production procedures of the physical model test: (a) boundary friction, (b) vibratory compaction, (c) water storage, (d) embedded sensor, (e) tunnel excavation, and (f) displacement meter arrangement.

Table 2: Water pressure loading mode for simulating the wetting-drying cycle effect.

N	p (MPa)	t_1 (min)	t_2 (min)
1	0.03	30	120
2	0.06	30	120
3	0.09	30	120
4	0.12	30	120
5	0.15	30	120
...	...	...	...

t_1: water pressure application time; t_2: drying time.

the same. For $N = 3 \sim 8$, the increments in each loading cycle are also 0.03 MPa.

3. Result and Analysis

3.1. Change in Pore Water Pressure. Figure 5 shows the water gushing process of the tunnel surrounding rock subjected to the alternation of wetting-drying. As the N is below 2, there was no seepage water observed on the excavation surface of the tunnel. When $N = 3$, a few drops of water began to leak out at the right of the tunnel vault, which were unevenly distributed. With the increase in N, it can be observed that more and more water droplets are seeped, and the infiltration region extended to the left and top of the tunnel vault. In the N range of $5 \sim 6$, the permeation was aggravated, which performed that the water was leaked out from the whole vault, and the infiltration region extended to the side wall. What is more, the water in some areas was flowed linearly. When N=7, lots of drips or linear water were flowed out from the whole vault and two sides wall, which mean that water inrush of tunnel was formed.

The pore water pressure will vary in each cycle of the wetting-drying process. Specifically, in each cycle, the pore water pressure increases firstly and then becomes stable. In the unstable stage, water in the surrounding rock is in a flowing and adjusting state and the tested pore water pressure will be influenced by the installing direction of the sensor. However, in the water stable stage, the tested value remains constant in general. Therefore, in order to reduce the error of data, the pore water pressure in the stable stage is mainly considered in this paper. The variation in pore water pressure with different wetting-drying cycle numbers is shown in Figure 6. With the increasing N, the pore water pressure presents an increasing trend in general. According to the changing trend of pore water pressure, three stages can be further identified: slightly increasing stage (1^{st}-2^{nd}), slowly increasing stage (2^{nd}–5^{th}), and sharply increasing stage (5^{th}–7^{th}), as shown in Figure 6. As N rises from 1 to 2, the value of pore water pressure at the location of the sensor increases slightly. In the N range of $2 \sim 5$, the pore water pressure presents a slowly increasing trend, which increases from 4.73 to 15.61 kPa, an increment of 10.88 kPa. At $N = 5 \sim 7$, the pore water pressure increases drastically, from 15.61 to 77.62 kPa, an increment of 62.01 kPa. It can be seen that the pore water pressure has an intrinsic connection with the wetting-drying cycle, but it is not a linear relationship.

During the process of the wetting-drying cycle, the frictional coefficient of minerals may decrease under the coupled

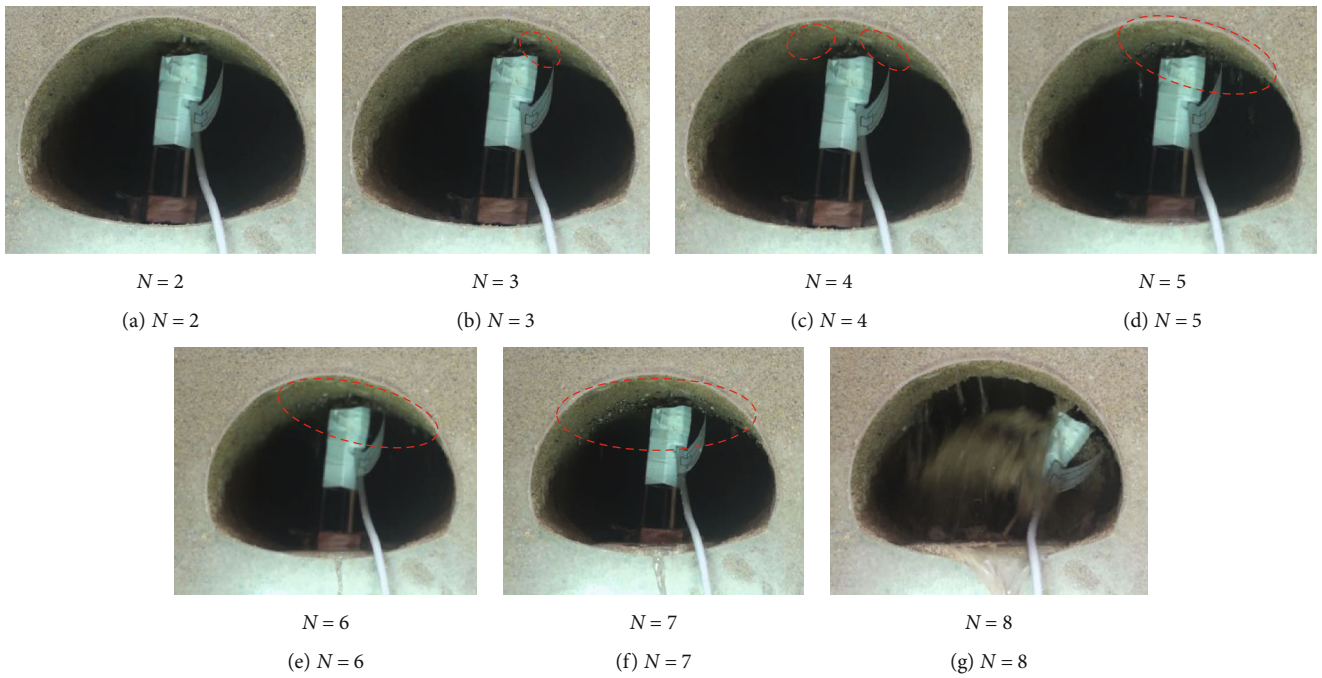

Figure 5: Water gushing process of tunnel surrounding rock subjected to the wetting-drying alternation (note: the dotted line denotes the area where seepage water appears).

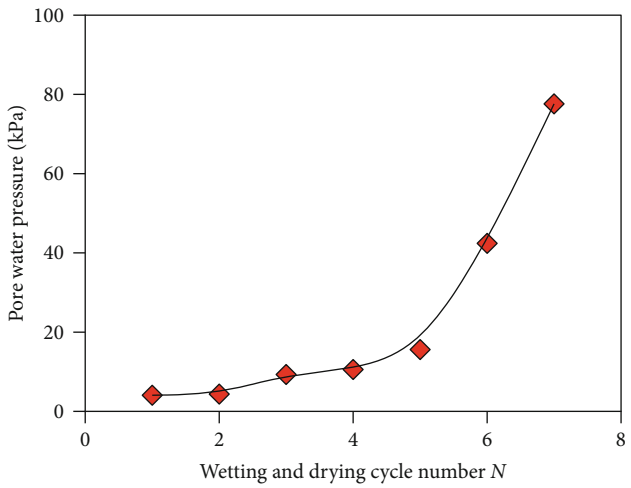

Figure 6: Effect of wetting-drying cycle number on the pore water pressure.

water-induced lubrication and bonding-weakening effects, resulting in the decrease of internal friction. As the consequence, the soluble substances in the surrounding rock mass, such as clay particles, are precipitated and separated, which leads to the increase in porosity of the surrounding rock and the improvement of permeability [30–32]. It should be mentioned that the initial porosity of the surrounding rock in the model is 8.73%. On the other hand, with the increase of water pressure, the seepage pressure of surrounding rock increases. However, the bearing capacity of the tunnel surrounding rock reduces [33]. What is more, this effect is aggravated due to the increase of cycle number and water pressure. It is easy to see that the pore water pressure increases nonlinearly, especially after $N = 5$.

3.2. Variations in Vertical Stress and Displacement. In order to further explore the effect of the wetting-drying cycle on the surrounding rock of the tunnel, this paper analyzes the change of the vertical stress on the two sides and baseplate (Figure 7), as well as the top-bottom approach (Figure 8) based on the experimental results. As shown in Figure 7, with the increasing N, the vertical stress on two sides of the tunnel wall also increases. More specifically, the vertical stress of the left wall increases from 150.64 to 172.84 kPa, by 14.74%. The right wall increases from 150.48 to 180.28 kPa, by 19.80%. This vertical stress evolution versus N could also be divided in three stages, which is similar to the variation of pore water pressure. However, the influence of the wetting-drying cycle on the vertical stress at baseplate of the tunnel is not significant. During the test, the vertical stress at the baseplate remains a low level. At the end of the experiment, this stress increases slightly after the occurrence of water inrush in the tunnel. These results all show that the karst water pressure will produce additional pressure on surrounding rock mass due to seepage. With the increase of N, the porosity of the surrounding rock mass increases and the seepage becomes more and more obvious. As a consequence, the in situ stress of the tunnel's main structure increases, so does the vertical stress of the surrounding rock mass on two sides of the tunnel. Some blocks at the top of the tunnel fall off when the water inrush appears. Therefore, the baseplate's vertical stress has the slight increase at the end of the experiment.

Figure 8 provides the variation in a top-bottom approach of the tunnel surrounding rock with different wetting-drying cycle numbers. It can be seen that with the increase in N, the

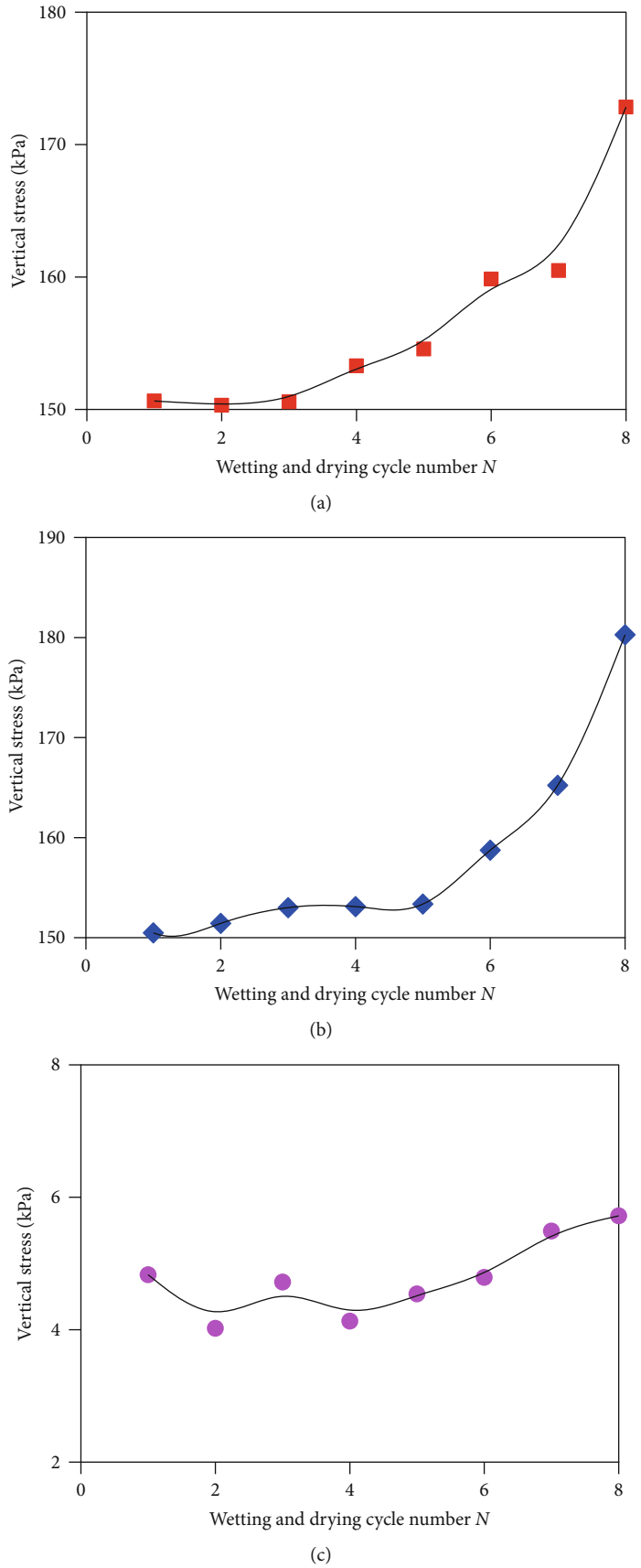

Figure 7: Influence of wetting-drying cycle number on vertical stress of the tunnel surrounding rock: (a) left wall, (b) right wall, and (c) baseplate.

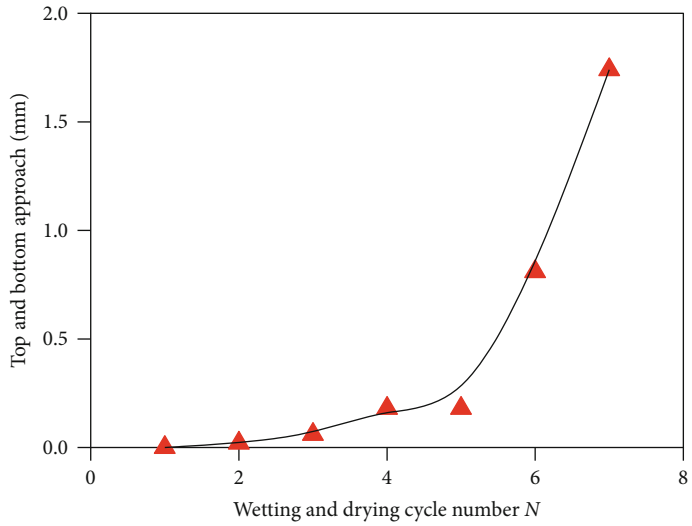

Figure 8: Effect of wetting-drying cycle number on a top and bottom approach of the tunnel surrounding rock.

tunnel top-bottom approach has an increasing trend. Besides, the evolution of the approach can be obviously divided into three stages. As N changes from 1 to 2, the approach has a slight increase, only 0.02 mm. In the N range of 2 ~ 5, the approach presents a slowly increasing trend, and only increases 0.16 mm. For $N = 5 \sim 7$, the approach increases drastically, from 0.18 to 1.74 mm, by 866.67%. For the following reasons, the wetting-drying cycle results in the increase in the porosity and corresponding moisture content of the vault's rock mass. And then, it indirectly causes an increase of in situ stress. In addition, the tunnel vault loses its original support when the tunnel excavation is completed. Hence, it has a downward trend under the action of in situ stress. With the increase of wetting-drying cycle number, the downward trend becomes even more pronounced. At the same time, the porosity of surrounding rock mass becomes larger, and the seepage path becomes broader, which ultimately leads to the destruction of the tunnel.

3.3. Superimposed Effect of Wetting-Drying Cycles and Water Pressure. During the model experiment, as the increase in N, the water pressure is also increased. When the water inrush occurs in tunnels, there is the effect of increasing water pressure, and also the results of strength degradation of the surrounding rock mass under the alternation of wetting-drying. Therefore, the superimposed effect of wetting-drying cycles and water pressure on the deformation of the surrounding rock was analyzed. Firstly, the stratum between the tunnel and karst caves is simplified into a theoretical model of clamped-clamped beam under uniformly distributed load, as shown in Figure 9. In this model, the height and span of beam is d and l, and the width is calculated as 1 m. In addition, the bulk density of the rock mass is γ, and the uniform water pressure is p.

Since the water storage structure is located at the top of the stratum, the maximum deflection of the stratum occurs in the middle of the span. According to the derivation of structural mechanics, a linear relationship between the maximum deflection δ_0 and the vertical distributed load $(p + \gamma d)$ could be obtained, which can be represented by Equation (1).

$$\delta_0 = \frac{(p + \gamma d) l^4}{384 E_c I}, \tag{1}$$

where E_c and I indicate the elasticity modulus and the moment of inertia, respectively.

According to Equation (1) and physical and mechanical properties of the sandstone specimens [34], the relationship between the maximum deflection and water pressure is shown in Figure 10. The water pressure indeed has a great influence on the maximum deflection. With the increase in water pressure, the maximum deflection increases gradually. However, the difference value between the two conditions increases with the increasing water pressure, and the area of this difference value represents the effect of wetting-drying alternation on maximum deflection.

In general, the water pressure indeed has a great influence on the stability of tunnel. But as the water pressure increases, the effect of the wetting-drying cycle increases obviously. Combined with our experimental scheme, when N is larger, the wetting-drying cycle also has a great influence, and the strength deterioration of the surrounding rock caused by the wetting-drying cycle cannot be ignored, which also illustrates the great significance to study the deterioration characteristics of the tunnel surrounding rock under the wetting-drying cycle.

4. UDEC Simulation

4.1. Numerical Model Construction. To verify the results of the physical experiments, numerical simulations were also adopted by using the Universal Discrete Element Code (UDEC). In a UDEC simulation, an assemblage of rigid and deformable block is expressed with the computational domain of interest through using a finite quantity of intersecting discontinuities. And the domain is treated as boundary conditions between blocks [35]. The fracture process can be represented by the change of the contact between blocks.

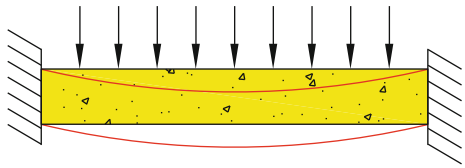

Figure 9: Displacement calculation sketch of the stratum between the tunnel and karst caves.

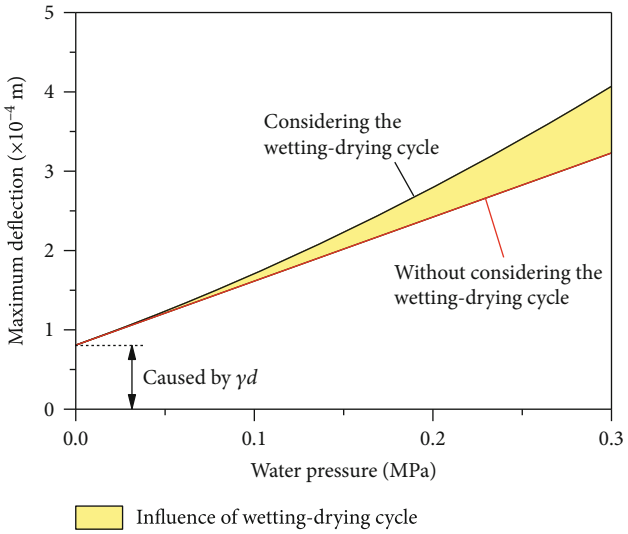

Figure 10: Relationship between the maximum deflection and water pressure.

In this simulation, based on the physical experiment results and the aid of UDEC, a numerical calculation method was proposed to study the water inrush, deformation, and failure mechanism under the action of the wetting-drying cycle. Figure 11 shows the basic calculation flow of numerical simulation, in which, P_i, ρ_i, and E_{ci} indicate the corresponding water pressure, density, and elasticity modulus as $N = i$. From the figure, we can see that the process of numerical simulation is basically consistent with that of the model experiment, except that the water pressure value of the first cycle is 0.5 MPa and each increment is by 0.5 MPa. In this paper, the basic parameters used for simulation were obtained by the previous studies and the experiment data [34, 36, 37]. The variations in compressive strength σ_c, peak strain ε_0, elasticity modulus E_c, and secant modulus E_{50} versus N can be expressed by the exponential function, as follows:

$$\begin{aligned} \sigma_c &= 83.40 - 1.24e^{N/3.68}, \\ \varepsilon_0 &= 1.06 + 1.91 \times 10^{-3} e^{(N+28.78)/7.76}, \\ E_c &= 10.04 - 0.98e^{N/7.10}, \\ E_{50} &= 6.39 - 0.2998e^{N/5.09}, \end{aligned} \tag{2}$$

Figure 12 demonstrates the degradation region iterative method based on the diffusion range. When $N = 1$, the osmotic diffusion boundary in the surrounding rock mass is

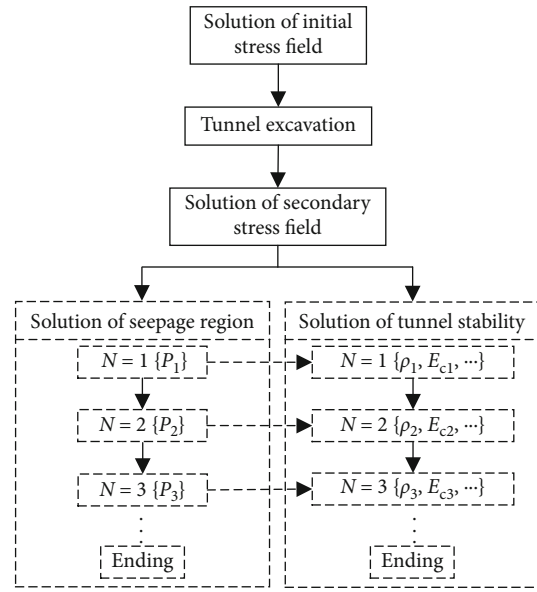

Figure 11: Calculation flow of the wetting-drying cycle.

1#, the diffusion region 'a' is substituted by $N = 1$ into the damage degradation model to calculate the physical and mechanical properties. When $N = 2$, the osmotic boundary diffuses to 2#. At this time, region 'b' uses $N = 1$ to substitute into the theoretical model for calculation, while region 'a' uses $N = 2$ for calculation. When $N = 3$, the osmotic boundary further diffuses to 3#. Then, region 'c' uses $N = 1$ to substitute into the theoretical model for calculation, region 'b' uses $N = 2$ for calculation, and region 'a' uses $N = 3$ for calculation. With the increase of N, the physical and mechanical properties of the damage deterioration zone are updated and assigned in this way. According to the measured data of the model test, the water inrush will be induced when the osmotic length reaches approximately 30% of the tunnel's length. Therefore, the UDEC simulation ends when the osmotic length reaches 30% of the tunnel length.

4.2. Analysis of the Simulation Results. The maximum and minimum principal stresses of the tunnel surrounding rock mass are also dominated by the effect of the wetting-drying cycle, as shown in Figures 13 and 14. With the increase of N, the maximum principal stress shows an increasing tendency, and the change of baseplate's maximum principal stress is more obvious. It can be seen in Figure 13 that the maximum principal stress between 40 and 50 MPa is in an area at the baseplate. Besides, the area gradually expands as N increase. While N has little effect on the maximum principal stress at the side wall and roof of the tunnel, as the maximum principal stress increases slightly in these places. With an increase in N, the minimum principal stress tends to decrease in the surrounding rock mass of the tunnel, but the change is not obvious. Figure 14 demonstrates the evolution of minimum principal stress. Before the appearance of water inrush, the minimum principal stress in the tunnel's surrounding rock mass primarily ranges from 0 to 10 MPa. The others would go below 10 MPa after the water inrush. It should be noted that, when $N = 5$, slender cracks appear

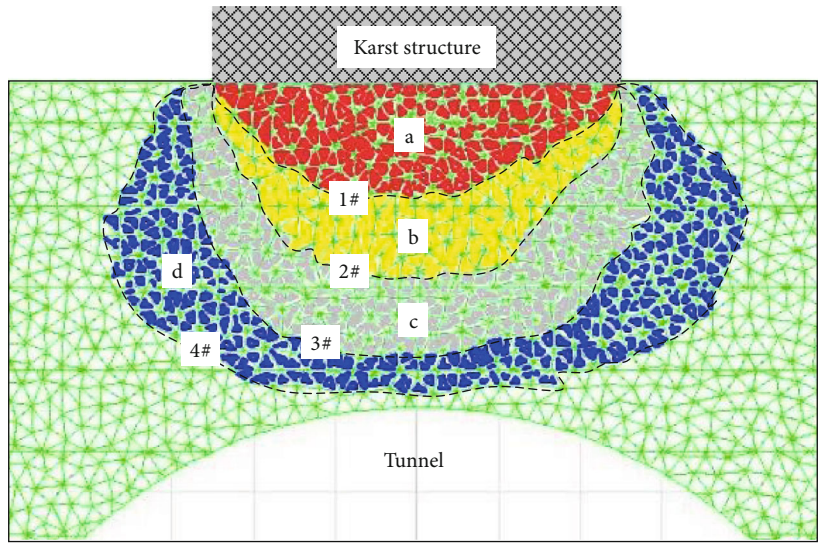

Figure 12: Degradation region iterative method based on the diffusion range.

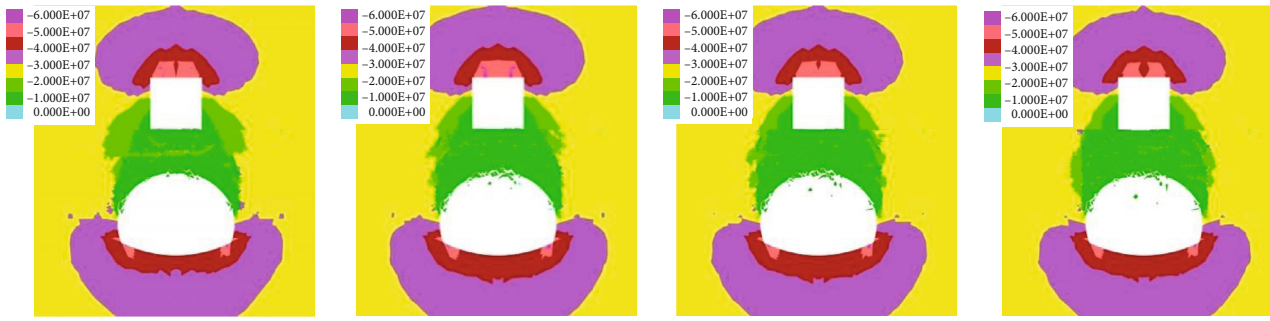

$N = 1$ $N = 4$ $N = 6$ $N_{cr} = 8$

(a) $N = 1$ (b) $N = 4$ (c) $N = 6$ (d) $N_{cr} = 8$

Figure 13: Evolution of maximum principal stress in the surrounding rock of the tunnel.

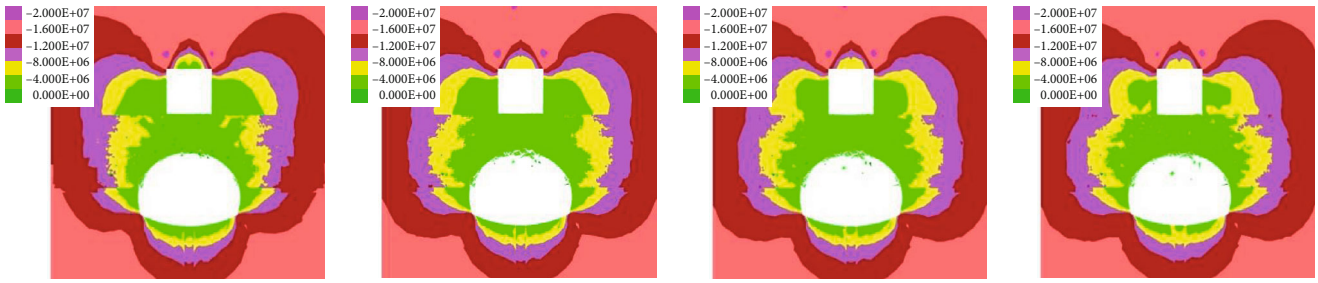

$N = 1$ $N = 4$ $N = 6$ $N_{cr} = 8$

(a) $N = 1$ (b) $N = 4$ (c) $N = 6$ (d) $N_{cr} = 8$

Figure 14: Evolution of minimum principal stress in the surrounding rock of the tunnel.

in the surrounding rock mass near the tunnel surface. With the increase in N, the cracks develop gradually. From these figures, we can also see that the surrounding rock mass exist obvious stress concentration, which manifests that the maximum and minimum principal stresses in the middle of the crack are slightly smaller while those at the end of the crack are larger.

Figure 15 shows the displacement evolution process of the surrounding rock mass of the tunnel, in which, the displacement is positive when pointing to the center of the

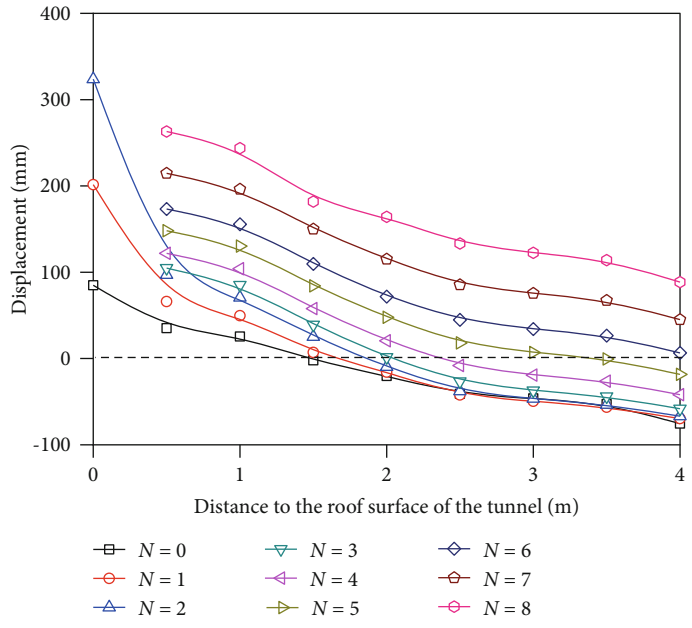

(a)

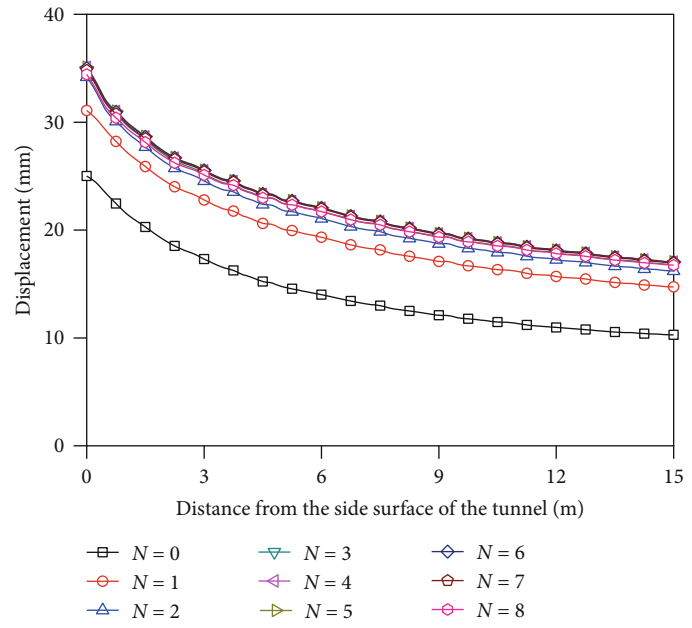

(b)

Figure 15: Continued.

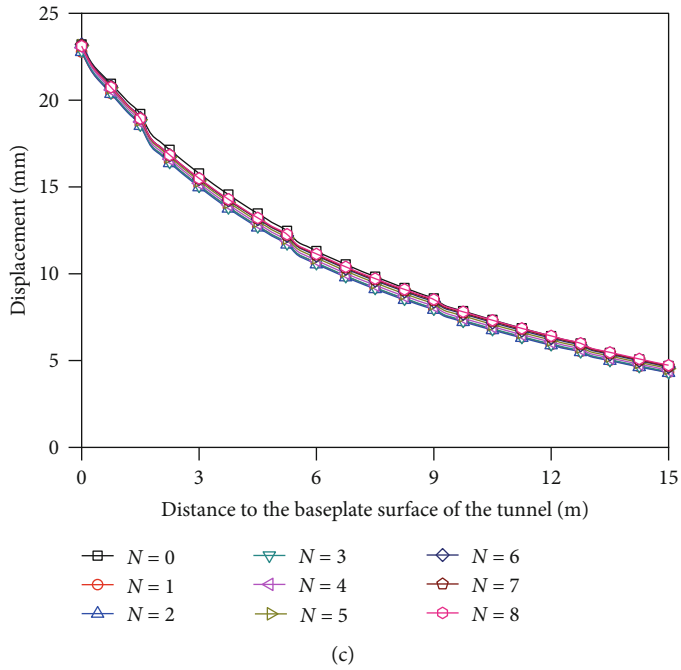

FIGURE 15: Displacement evolution process of the surrounding rock of the tunnel: (a) tunnel roof, (b) tunnel side wall, and (c) tunnel baseplate.

tunnel. It can be seen that all parts of the tunnel produce a positive displacement toward the center of the tunnel. As for the effect of position, with an increase in the distance from the measuring point to the surface of the tunnel, the displacement of the measuring point decreases gradually. On the other hand, the maximum displacement of the surrounding rock mass varies greatly at different positions. More specifically, the displacement of the surrounding rock mass at the tunnel roof is the largest, which reaches 243.78 mm, and the displacement at the tunnel side wall is 35.00 mm, while the displacement at the tunnel floor is the smallest, only 23.00 mm. As for the effect of the wetting-drying cycle, with the increase in N, the displacement of the surrounding rock mass at the top of the tunnel increases significantly, the displacement of the side wall increases less obviously, and the displacement at the baseplate basically hardly change at all. Taking the measuring point 1 m away from the surface of the tunnel roof as an example, the displacement at $N = 1$, 4, 6, and 8 is 49.67, 104.00, 155.63, and 243.78 mm, respectively, which increases by 390.80% under the effect of the wetting-drying cycle.

Figure 16 reflects the contrast of destruction between physical experiment and numerical simulation at $N = 8$. The figures directly reflect the tunnel roof damage serious. While the surrounding rock mass in the two side walls of the tunnel has a slight damage. Physical experiment and numerical simulation have a great consistency, which can be reasonably explained by the change of previous results. For example, it can be seen from Figure 15(a) that the maximum displacement of the tunnel roof reaches to 323.81 mm when $N = 2$, and it occurs 0.5 m away from the surface of the tunnel roof when $N = 3$. These results show that the rock mass of the tunnel roof falls off in a certain thickness; in other words, the surrounding rock mass is destroyed to some extent.

5. Conclusions

In this study, taking the working condition of the Liupanshan tunnel as the background, physical model tests and UDEC simulations were set up to explore the process and mechanism of tunnel water inrush in the karst area under the wetting-drying cycle. Based on these results, some conclusions can be obtained as follows:

(1) Based on the physical and mechanical properties of sandstone, a similar material with optimal proportion is developed, which is composed of river sand, talcum powder, paraffin, and hydraulic oil at a mass ratio of 23.0 : 3.5 : 1.5 : 1.0. And the physical experiment system is set up by using this similar material

(2) The wetting-drying cycle has a negative effect on the mechanical property of the tunnel surrounding mass. With the increase in N, the pore water pressure, vertical stress, and top-bottom approach of the tunnel surrounding rock increase gradually. In addition, these trends have a similar change law, which successively show three stages of slight, slow, and sharp variation

(3) The wetting-drying cycle is an important factor resulting in the failure and instability of tunnel surrounding rock. Using numerical simulation, the effects of wetting-drying cycle were further discussed. The wetting-drying cycle weakens the stability of the

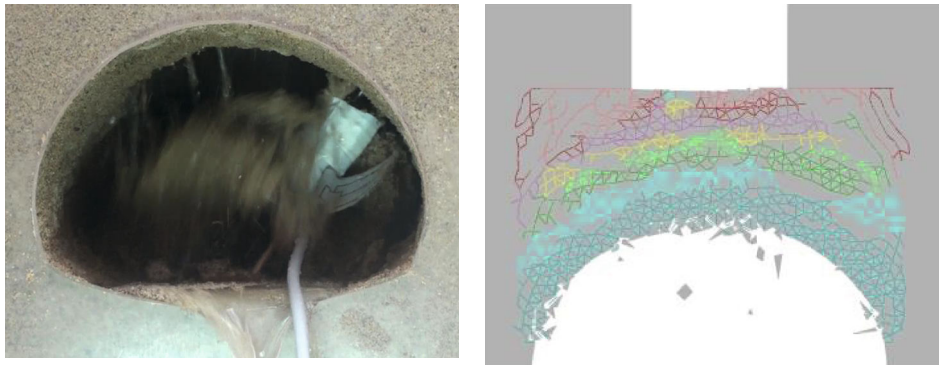

(a) (b)

Figure 16: Contrast of destruction between (a) physical experiment and (b) UDEC simulation ($N = 8$).

tunnel, especially after the 5th cycle. The failure process gradually occurs from the roof to side wall, while the baseplate changes slightly

In this study, the influence of a wetting-drying cycle on tunnel stability was investigated, especially for stress and displacement evolutions. In order to further understand the influence, more experimental and numerical investigations will be conducted by advanced techniques (such as DIC) to study the strain evolutions of the tunnel surrounding rock.

Data Availability

The data used to support the findings of this study are available from the corresponding author upon request.

Conflicts of Interest

The authors declare no conflict of interest.

Acknowledgments

This study is financed by the National Natural Science Foundation of China (Nos. 51704279, 51734009, and 51579239) and the Natural Science Foundation of Jiangsu Province of China (No. BK20170270). The authors also like to acknowledge the Professor Haibo Bai of China University of Mining and Technology for his help in rock identification.

References

[1] J. Yu, X. Chen, Y. Y. Cai, and H. Li, "Triaxial test research on mechanical properties and permeability of sandstone with a single joint filled with gypsum," *KSCE Journal of Civil Engineering*, vol. 20, no. 6, pp. 2243–2252, 2016.

[2] Q. Yin, G. Ma, H. Jing et al., "Hydraulic properties of 3d rough-walled fractures during shearing: an experimental study," *Journal of Hydrology*, vol. 555, pp. 169–184, 2017.

[3] D. Ma, H. Duan, J. Liu, X. Li, and Z. Zhou, "The role of gangue on the mitigation of mining-induced hazards and environmental pollution: an experimental investigation," *Science of the Total Environment*, vol. 664, pp. 436–448, 2019.

[4] E. Kim and H. Changani, "Effect of water saturation and loading rate on the mechanical properties of red and buff sandstones," *International Journal of Rock Mechanics and Mining Sciences*, vol. 88, pp. 23–28, 2016.

[5] T. Inoue, S. Yamaguchi, and J. M. Nelson, "The effect of wet-dry weathering on the rate of bedrock river channel erosion by saltating gravel," *Geomorphology*, vol. 285, pp. 152–161, 2017.

[6] Z. Zhou, X. Cai, D. Ma, L. Chen, S. Wang, and L. Tan, "Dynamic tensile properties of sandstone subjected to wetting and drying cycles," *Construction and Building Materials*, vol. 182, pp. 215–232, 2018.

[7] Z. Qin, X. Chen, and H. Fu, "Damage features of altered rock subjected to drying-wetting cycles," *Advances in Civil Engineering*, vol. 2018, 10 pages, 2018.

[8] X. Chen, J. Yu, C.'. Tang, H. Li, and S. Wang, "Experimental and numerical investigation of permeability evolution with damage of sandstone under triaxial compression," *Rock Mechanics and Rock Engineering*, vol. 50, no. 6, pp. 1529–1549, 2017.

[9] E. Rojas, J. Horta, T. López-Lara, and J. B. Hernández, "A probabilistic solid-porous model to determine the shear strength of unsaturated soils," *Probabilistic Engineering Mechanics*, vol. 26, no. 3, pp. 481–491, 2011.

[10] B. Y. Zhang, J. H. Zhang, and G. L. Sun, "Deformation and shear strength of rockfill materials composed of soft siltstones subjected to stress, cyclical drying/wetting and temperature variations," *Engineering Geology*, vol. 190, no. 2, pp. 87–97, 2015.

[11] P. A. Hale and A. Shakoor, "A laboratory investigation of the effects of cyclic heating and cooling, wetting and drying, and freezing and thawing on the compressive strength of selected sandstones," *Environmental and Engineering Geoscience*, vol. 9, no. 2, pp. 117–130, 2003.

[12] P. Sumner and M. Loubser, "Experimental sandstone weathering using different wetting and drying moisture amplitudes," *Earth Surface Processes and Landforms*, vol. 33, no. 6, pp. 985–990, 2008.

[13] M. Coombes and L. Naylor, "Rock warming and drying under simulated intertidal conditions, part II: weathering and biological influences on evaporative cooling and near-surface micro-climatic conditions as an example of biogeomorphic ecosystem engineering," *Earth Surface Processes and Landforms*, vol. 37, no. 1, pp. 100–118, 2012.

[14] F. Jeng, M. Lin, and T. Huang, "Wetting deterioration of soft sandstone-microscopic insights," in *ISRM International Symposium*, pp. 525–540, Melbourne, Australia, November 2000.

[15] D. Li, L. N. Y. Wong, G. Liu, and X. Zhang, "Influence of water content and anisotropy on the strength and deformability of low porosity meta-sedimentary rocks under triaxial compression," *Engineering Geology*, vol. 126, pp. 46–66, 2012.

[16] J. Yu, T. B. Li, J. Z. Zhang, and Y. Y. Cai, "Stress characteristics of surrounding rocks for inner water exosmosis in high-pressure hydraulic tunnels," *Journal of Central South University*, vol. 21, no. 7, pp. 2970–2976, 2014.

[17] Y. Nara, H. Yamanaka, Y. Oe, and K. Kaneko, "Influence of temperature and water on subcritical crack growth parameters and long-term strength for igneous rocks," *Geophysical Journal International*, vol. 193, no. 1, pp. 47–60, 2013.

[18] D. Ma, J. Wang, X. Cai et al., "Effects of height/diameter ratio on failure and damage properties of granite under coupled bending and splitting deformation," *Engineering Fracture Mechanics*, vol. 220, p. 106640, 2019.

[19] S. Yin, J. Zhang, and D. Liu, "A study of mine water inrushes by measurements of in situ stress and rock failures," *Natural Hazards*, vol. 79, no. 3, pp. 1961–1979, 2015.

[20] D. Ma, H. Duan, X. Li, Z. Li, Z. Zhou, and T. Li, "Effects of seepage-induced erosion on nonlinear hydraulic properties of broken red sandstones," *Tunneling and Underground Space Technology*, vol. 91, p. 102993, 2019.

[21] D. Ma, J. Wang, and Z. Li, "Effect of particle erosion on mining-induced water inrush hazard of karst collapse pillar," *Environmental Science and Pollution Research*, vol. 26, no. 19, pp. 19719–19728, 2019.

[22] B. Yao, J. Wei, D. Wang, D. Ma, and Z. Chen, "Numerical study of seepage property of karst collapse columns under particle migration," *Computer Modeling in Engineering and Sciences*, vol. 91, no. 2, pp. 81–100, 2013.

[23] Z. Zhou, X. Cai, D. Ma et al., "Water saturation effects on dynamic fracture behavior of sandstone," *International Journal of Rock Mechanics and Mining Sciences*, vol. 114, pp. 46–61, 2019.

[24] M. N. Bidgoli and L. Jing, "Water pressure effects on strength and deformability of fractured rocks under low confining pressures," *Rock Mechanics and Rock Engineering*, vol. 48, no. 3, pp. 971–985, 2015.

[25] People's Republic of China National Standard, *Engineering Rock Test Method Standard (GB/T 50266–2013)*, China Planning Publishing House, Beijing, 2013.

[26] Z. Weishen, L. Yong, L. Shucai, W. Shugang, and Z. Qianbing, "Quasi-three-dimensional physical model tests on a cavern complex under high in-situ stresses," *International Journal of Rock Mechanics and Mining Sciences*, vol. 48, no. 2, pp. 199–209, 2011.

[27] L. Liu, Z. Li, X. Liu, and Y. Li, "Frost front research of a cold-region tunnel considering ventilation based on a physical model test," *Tunnelling and Underground Space Technology*, vol. 77, pp. 261–279, 2018.

[28] Q. Tian, J. Zhang, and Y. Zhang, "Similar simulation experiment of expressway tunnel in karst area," *Construction and Building Materials*, vol. 176, pp. 1–13, 2018.

[29] X. Yue, Y. Xie, and Y. Xie, "The deformation characteristics of weak foundation with high back siltation in the immersed tunnel," *Advances in Materials Science and Engineering*, vol. 2018, Article ID 6538764, 14 pages, 2018.

[30] E. M. van Eeckhout, "The mechanisms of strength reduction due to moisture in coal mine shales," *International Journal of Rock Mechanics and Mining Sciences*, vol. 13, no. 2, pp. 61–67, 1976.

[31] W. Liu and Z.-h. Zhang, "Experimental characterization and quantitative evaluation of slaking for strongly weathered mudstone under cyclic wetting-drying condition," *Arabian Journal of Geoscience*, vol. 13, no. 2, 2020.

[32] Z. Zhou, X. Cai, D. Ma, W. Cao, L. Chen, and J. Zhou, "Effects of water content on fracture and mechanical behavior of sandstone with a low clay mineral content," *Engineering Fracture Mechanics*, vol. 193, pp. 47–65, 2018.

[33] D. Pan, S. Li, Z. Xu et al., "Model tests and numerical analysis for water inrush caused by karst caves filled with confined water in tunnels," *Chinese Journal of Geotechnical Engineering*, vol. 40, no. 5, pp. 828–836, 2018.

[34] B. Meng, H. Jing, W. Zhu, and H. Su, "Influences of saturation and wetting-drying cycle on mechanical performances of argillaceous limestones from Liupanshan tunnel, China," *Advances in Materials Science and Engineering*, vol. 2019, 10 pages, 2019.

[35] S.-Q. Yang, M. Chen, H.-W. Jing, K.-F. Chen, and B. Meng, "A case study on large deformation failure mechanism of deep soft rock roadway in Xin'An coal mine, China," *Engineering Geology*, vol. 217, pp. 89–101, 2017.

[36] X. Deng, D. Yuan, D. Yang, and C. Zhang, "Back Analysis of Geomechanical Parameters of Rock Masses Based on Seepage-Stress Coupled Analysis," *Mathematical Problems in Engineering*, vol. 2017, 13 pages, 2017.

[37] L. Li and H.-H. Liu, "EDZ formation and associated hydromechanical behaviour around ED-B tunnel: a numerical study based on a two-part Hooke's model (TPHM)," *KSCE Journal of Civil Engineering*, vol. 19, no. 1, pp. 318–331, 2015.